

Chapter 9

Si Nanopowder for Photoluminescence and Hydrogen Generation Materials



Yuki Kobayashi and Hikaru Kobayashi

Abstract Si nanopowder fabricated from Si swarf using the beads milling method exhibits two kinds of photoluminescence (PL), green-PL and blue-PL. Green-PL arises from band-to-band transition of Si nanopowder with band-gap enlarged by the quantum confinement effect. Blue-PL, on the other hand, is attributable to adsorbed 9,10-dimethylanthracene (DMA) impurity in hexane because the structure of the observed PL spectra is nearly identical to that of DMA solvent. The peaked PL spectra arise from vibronic interaction of DMA, and nearly the identical separation energies between the neighboring peaks correspond to the vibrational energy of DMA in the electronic ground-state. The PL intensity of DMA is enhanced by 60,000 times due to adsorption of DMA on Si nanopowder. For excitation photon energies higher than 4.0 eV, new peaks appear in the energy region higher than the (0, 0) band, attributable to transition from vibrational excited-states.

Si nanopowder reacts with water in the neutral pH region between 7 and 9. The hydrogen generation rate strongly depends on pH, while pH doesn't change after the reaction. Si nanopowder reacts with OH⁻ ions, generating hydrogen, SiO₂, and electrons in the SiO₂ conduction band. Electrons are accepted by water molecules, generating hydrogen and OH⁻ ions. Since OH⁻ ions act as a catalyst, the hydrogen generation rate greatly increases with pH. The generated hydrogen volume vs. the reaction time follows a logarithmic relationship, indicating that migration of OH⁻ ions through the SiO₂ layer is the rate-determining step. The hydrogen generation reaction stops when the SiO₂ thickness reaches to ~5 nm.

Keywords PL enhancement · Vibrational excited-state · Neutral water · Hydroxyl ions · Internal hydrogen generation · Oxidative stress

Y. Kobayashi · H. Kobayashi (✉)

Institute of Scientific and Industrial Research, Osaka University, Ibaraki, Osaka, Japan

e-mail: h.kobayashi@sanken.osaka-u.ac.jp

© Springer Nature Singapore Pte Ltd. 2020

T. Onishi (ed.), *Theoretical Chemistry for Advanced Nanomaterials*,

https://doi.org/10.1007/978-981-15-0006-0_9

9.1 Photoluminescence From Si Nanostructures

9.1.1 Introduction

Si is a nonpoisonous material, and thus, its photoluminescence (PL) phenomenon is applicable to biology [1]. PL from Si nanoparticles is attributed to (i) intrinsic band-to-band transition [2, 3] and (ii) extrinsic transition involving states such as defect states in an oxide layer [3, 4]. For case (i), the PL energy depends on the size of Si nanoparticles because the band-gap energy strongly depends on the size due to the quantum confinement effect [5, 6]. For example, the energy shift of the PL peaks by oxidation of Si nanoparticles results from case (i) because oxidation decreases the size of Si nanoparticles by the formation of SiO₂ [2, 3]. For case (ii), on the other hand, the PL energies are less dependent or independent of the nanoparticle size [3, 4].

Trave et al. [6] fabricated Si nanoparticles by the laser pyrolysis method and found that the PL intensity of as-deposited nanoparticles was weak, but it increased after thermal oxidation at temperatures between 700 and 1000 °C accompanied by blue shift to the wavelength region between 800 and 900 nm. Kang et al. [2] showed that using the oxidation method which could control the size of Si nanoparticles, the PL emission color could be varied in the wide wavelength range between red and blue. For Si nanoparticles produced using the pulsed laser ablation method in liquid, a PL peak was observed at ~500 nm [7] or 450 and 600 nm [8]. Si nanoparticles which exhibited PL were also formed by the use of the laser ablation method in helium gas [9]. Si nanoparticles of ~3 nm size were fabricated by implantation of Si⁺ ions onto SiO₂, and the PL peak was observed in the 750~950 nm wavelength region [10]. Si nanoparticles embedded in silicon oxide were formed by the rf co-sputtering method, and their PL spectra were greatly changed by heat treatment up to 1100 °C [8]. Using ball-milling of graphite and SiO₂ powder, Si nanoparticles with PL emission in the broad wavelength region between 650 and 900 nm were fabricated [11]. For Si nanoparticles fabricated using ball milling of graphite and SiO₂ powder, broad PL spectra were observed in the wavelength region between 650 and 900 nm [12].

Several researchers investigated effects of adsorbates on Si nanoparticles on PL behavior. Ryabechikov et al. [13] showed that adsorption of alkyl groups caused blue shift of the PL peak accompanied with broadening of the peak and attributed the phenomenon to prevention of energy transfer from small to large Si nanoparticles by adsorption. For phenyl-passivated Si nanoparticles in hexane, Imamura et al. [14] reported three-peaked PL spectra (~3.52, ~3.68, and ~3.85 eV) which did not depend on excitation photon energies. Fang et al. [15] observed enhancement of PL from adsorbed porphyrin on Ag nanoparticle-covered Si surfaces and attributed the enhancement to the resonant excitation by local surface plasmons and to the increased radiative decay rate. We observed peaked structure in the PL spectra for Si nanopowder in hexane and attributed it to 9,10-dimethylanthracene (DMA) adsorbed on the surface by which the PL intensity was greatly enhanced [16, 17].

9.1.2 Experiments

Si swarf generated during slicing of Si ingots by use of the fixed-abrasive wire saw method was used as a starting material. After cleaning with organic solvent to remove coolant and other organic species, Si swarf was milled with a ball mill apparatus followed by beads milling with zirconia beads [16–19]. For one-step beads milling, 0.5 μm diameter beads were used, while for two-step beads milling, subsequent milling was performed with 0.3 μm beads. The following two different methods were employed for production of green-PL and blue-PL Si nanopowder: To obtain green-PL Si nanopowder, fabricated nanopowder was etched with an HF solution, followed by centrifugation and filtration, and then, it was immersed in ethanol. For fabrication of blue-PL Si nanopowder, milled swarf was filtered using a Teflon membrane filter, followed by immersion in hexane solvent.

Transmission electron microscopy (TEM) measurements were performed using an EM-3000F (JEOL) microscope with 300 keV incident electrons. X-ray diffraction (XRD) measurements were carried out by use of a Rigaku SmartLab diffractometer. Photoluminescence (PL) spectra were recorded using a Hitachi High-Technologies Corporation F-7000 spectrometer. Ultraviolet and visible light (UV-Vis) absorption spectra were measured by use of a JASCO V-570 spectrometer. Time-dissolved PL measurements were carried out using a HORIBA DeltaFlex photometer.

9.1.3 Results and Discussion

9.1.3.1 Structure of Si Nanopowder

Figure 9.1a shows the TEM micrograph of Si nanopowder fabricated by the one-step beads milling method from Si swarf. The TEM observation was performed after etching with an HF solution to remove amorphous SiO_2 . Many crystallites with polygonal shapes and sizes less than 10 nm are clearly observed.

Fig. 9.1 TEM micrographs of Si nanopowder fabricated from Si swarf using the following beads milling methods: (a) one-step milling, (b) two-step milling

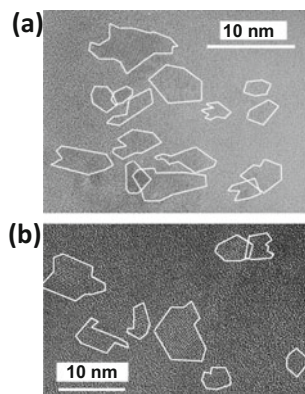


Fig. 9.2 XRD patterns of Si swarf before (a) and after beads milling using the following methods: (b) one-step milling, (c) two-step milling

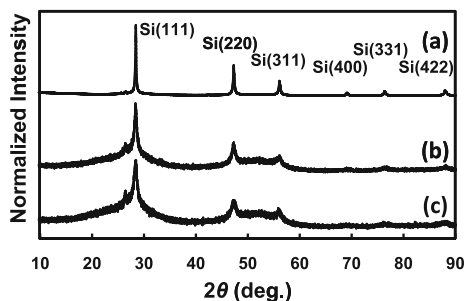


Fig. 9.3 Volume distribution of the crystallite size of Si nanopowder fabricated from Si swarf using the following methods: (a) one-step beads milling, (b) two-step beads milling

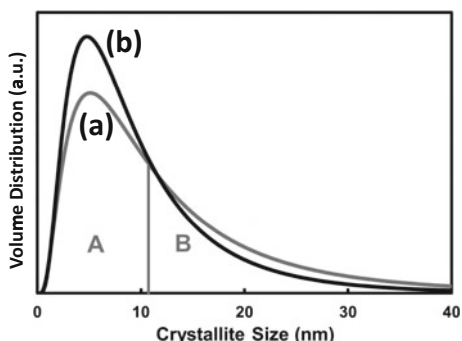


Figure 9.2 shows the XRD patterns of Si swarf before (pattern a) and after one-step (pattern b) and two-step (pattern c) beads milling. The intense peaks at 28.4 , 47.5 , and 56.2° are attributable to (111), (220), and (311) orientations of Si nanopowder. After beads milling, all the diffraction peaks due to Si observed before milling are present with nearly the same intensity ratio, but the widths of the peaks are considerably increased, indicating that the average crystallite sizes are greatly decreased.

From the analysis of the shape of the Si(111) XRD peak, the volume distribution of Si nanopowder (i.e., distribution of the volume of Si nanoparticles vs. the diameter assuming the spherical shape) obtained using the theoretical diffraction line profile from spherical crystallites with lognormal size distribution (SLN profile) method [20] is shown in Fig. 9.3. For one-step milling, the maximum of the volume distributions (i.e., mode diameter) is present at 5.2 nm. The median diameter for the volume distribution (i.e., the vertical line by which two regions, A and B, is divided into the same areas) is estimated to be 10.5 nm and the average diameter to be 13.2 nm. For two-step milling, the mode diameter, the median diameter, and the average diameter are determined to be 4.8, 8.4, and 10.2 nm, respectively.

9.1.3.2 Photoluminescence from Si Nanopowder

Figure 9.4 shows the photos of the solutions containing blue-PL and green-PL Si nanopowders, observed under 365 nm black light irradiation. Si nanopowder was

Fig. 9.4 Photos of Si nanopowder in the following solvents under black light irradiation: (a) Si nanopowder without HF etching in hexane, (b) Si nanopowder with HF etching in ethanol. Photo c is for hexane without Si nanopowder

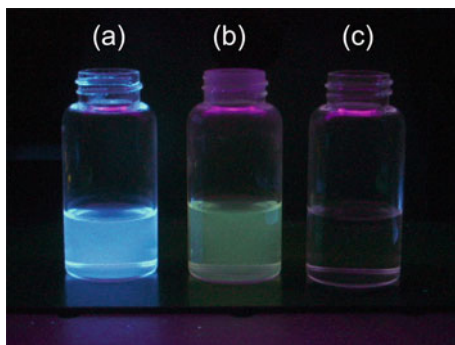
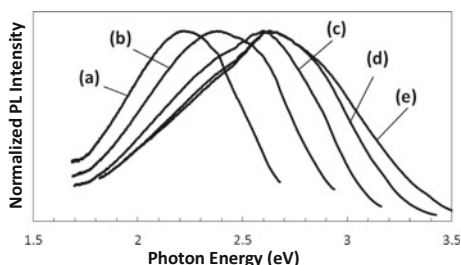


Fig. 9.5 PL spectra of green-PL Si nanopowder in ethanol with HF etching observed under the following excitation energies: (a) 2.76 eV, (b) 3.02 eV, (c) 3.26 eV, (d) 3.54 eV, (e) 3.76 eV



fabricated using the one-step beads milling method from Si swarf. It is clearly seen that PL color strongly depends on the treatments carried out after fabrication of Si nanopowder. Si nanopowder without HF etching in hexane shows blue-PL (Fig. 9.4a) while that with HF etching in ethanol exhibits green-PL (Fig. 9.4b). It is noted that hexane without Si nanopowder doesn't show PL (Fig. 9.4c).

Green-Photoluminescence-Emitting Si Nanopowder

Figure 9.5 shows the PL spectra for green-PL Si nanopowder. Only one broad peak is observed in the spectra, and the peak maximum shifts in the higher energy direction by an increase in the excitation photon energy. The width of the peak increases with the excitation energy (i.e., incident light energy). It should be noted that Si nanopowder includes various size crystallites as shown in Fig. 9.3. With low excitation energy, only large size Si crystallites with narrow band-gap energies are excited, followed by low energy PL (Fig. 9.6a). With high excitation energy, on the other hand, smaller Si nanopowder with higher band-gap energies can also be excited, and thus, higher energy PL is exhibited (Fig. 9.6b). The broader structure of the PL spectra results from wider distribution of PL-emitting Si nanopowder with various band-gap energies, e.g., 2.2 eV band-gap for 2.4 nm diameter and 1.7 eV for 4.5 nm diameter [5, 6].

Figure 9.7 shows the PL spectra for one-step beads milled Si nanopowder (spectrum a) and two-step milled Si nanopowder (spectrum b). The maximum of the PL peak for one-step beads milled Si nanopowder is located at 2.60 eV while that for two-step beads milled Si nanopowder is present at 2.91 eV. Since two-step

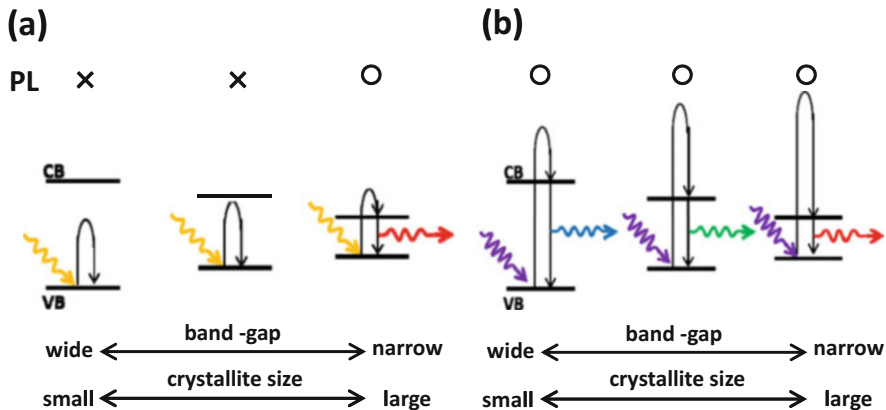
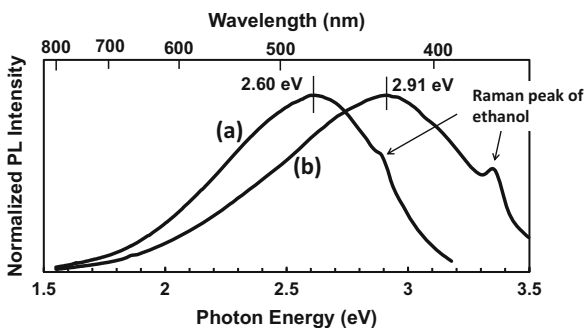


Fig. 9.6 Schematics to explain the relationship between the PL characteristics and the excitation energy: (a) low excitation energy, (b) high excitation energy

Fig. 9.7 PL spectra for green-PL Si nanopowder fabricated with the following methods: (a) one-step beads milling, (b) two-step beads milling



beads milled Si nanopowder possesses higher band-gap energies due to the quantum confinement effect, this result also gives the evidence that green-PL arises from band-to-band transition of Si nanopowder.

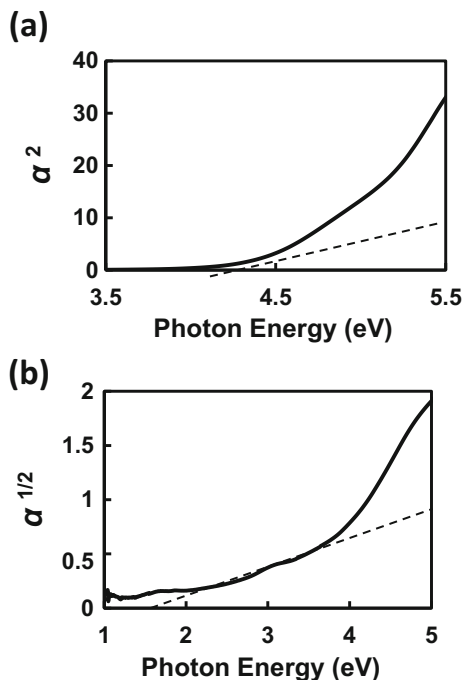
Assuming the free electron model for valence and conduction bands of Si nanopowder and using the indirect band-gap energy, $E_{g, \text{indi}}$, and direct band-gap energy, $E_{g, \text{di}}$, the absorption coefficient, α , is written as

$$\alpha^2 \propto h\nu - E_{g, \text{di}}, \tag{9.1}$$

$$\alpha^{1/2} \propto h\nu - E_{g, \text{indi}}, \tag{9.2}$$

where $h\nu$ is the incident photon energy. The plots for green-PL Si nanopowder using Eq. (9.1) and (9.2) are shown in Fig. 9.8a and b, respectively. Both the plots aren't

Fig. 9.8 Plots for estimation of the band-gap energies of Si nanopowder: (a) α^2 vs. $h\nu$ (α , absorption coefficient; $h\nu$, photon energy) plot for estimation of indirect band-gap energy, (b) $\alpha^{1/2}$ vs. $h\nu$ plot for estimation of the direct band-gap energy



linear but curves with the curvature increasing with the energy. These nonlinear plots result from presence of Si nanopowder with various sizes (cf. Fig. 9.3). From the intercept of the plot with the energy axis, the minimum of the indirect band-gap energy of Si nanopowder is determined to be 1.3 eV, which corresponds to the diameter of 6~8 nm [21]. On the other hand, the minimum of the direct band-gap energy is estimated to be 4.1 eV (cf. direct band-gap energy of crystalline Si: 3.4 eV [22]).

Blue-Photoluminescence-Emitting Si Nanopowder

Figure 9.9 shows the PL spectra of blue-emission Si nanopowder fabricated by the one-step milling method. Four peaks are clearly observed at 2.54, 2.72, 2.91, and 3.10 eV, and these peak energies don't change at all by changing the excitation photon energy from 3.17 eV (spectrum a) to 3.50 eV (spectrum c). This result indicates that blue-PL arises from a single source. The PL spectra of Si nanopowder coincide with that of DMA (spectrum d). These results show that PL emission results from adsorbed DMA on Si nanopowder surfaces. (Low concentration DMA is present in hexane as an impurity.) The PL emission is attributable to $\pi - \pi_*$ transition of DMA and the peaked structure to the vibronic bands with the total symmetric breathing vibrational mode [23].

Figure 9.10 shows the PL spectra of hexane containing Si nanopowder before (spectrum a) and after (spectrum b) addition of an HNO_3 plus HF solution. The HNO_3 plus HF solution dissolves Si nanopowder [24], and after addition,

Fig. 9.9 PL spectra of blue-PL Si nanopowder observed with the following excitation energies: (a) 3.17 eV, (b) 3.35 eV, (c) 3.50 eV. Spectrum d is for free DMS molecules for comparison

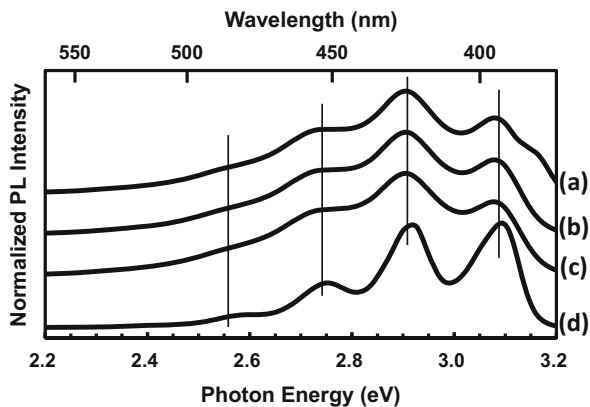
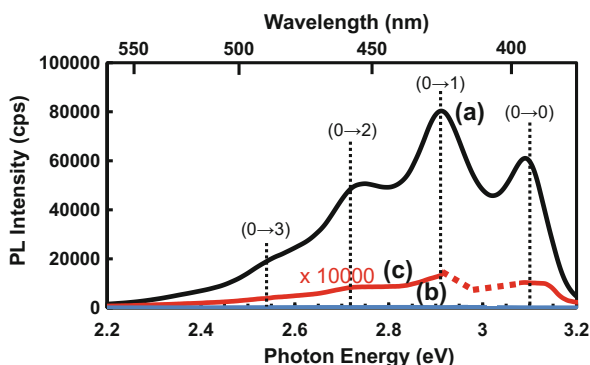


Fig. 9.10 PL spectra for blue-PL Si nanopowder fabricated using the one-step beads milling method before (a) and after (b) addition of an HNO_3 +HF solution. Spectrum c is 10,000 times enlargement of spectrum b



the PL intensity greatly decreases, indicating that adsorption of DMA on Si nanopowder greatly enhances the PL intensity. The low intensity PL observed after addition of $\text{HF}+\text{HNO}_3$ is probably due to undissolved Si nanopowder stabilized by adsorbed DMA. The PL intensity of a DMA-containing hexane solution without Si nanopowder don't change at all by addition of HF plus HNO_3 , showing that the $\text{HF}+\text{HNO}_3$ solution doesn't react with DMA (i.e., no chemical reaction). Spectrum c is observed after concentration of DMA in hexane solutions by 10,000 times by evaporation. Comparison of spectrum a with spectrum c demonstrates that the PL intensity of DMA is enhanced by $\sim 60,000$ times by the presence of Si nanopowder.

Figure 9.11 shows the absorption spectra of blue-PL Si nanopowder in hexane. For both the spectra, the absorption background due to hexane solvent is subtracted. In the presence of Si nanopowder in hexane (spectrum a), the peaked structure is observed, and it is attributed to absorption by DMA adsorbed on Si nanopowder. The peaked structure in the absorption spectrum due to adsorbed DMA disappears by addition of an $\text{HF}+\text{HNO}_3$ solution in hexane containing Si nanopowder (spectrum b), clearly showing that the peaked structure arises from DMA adsorbed on Si nanopowder, but not from free DMA dissolved in hexane. It is confirmed that the

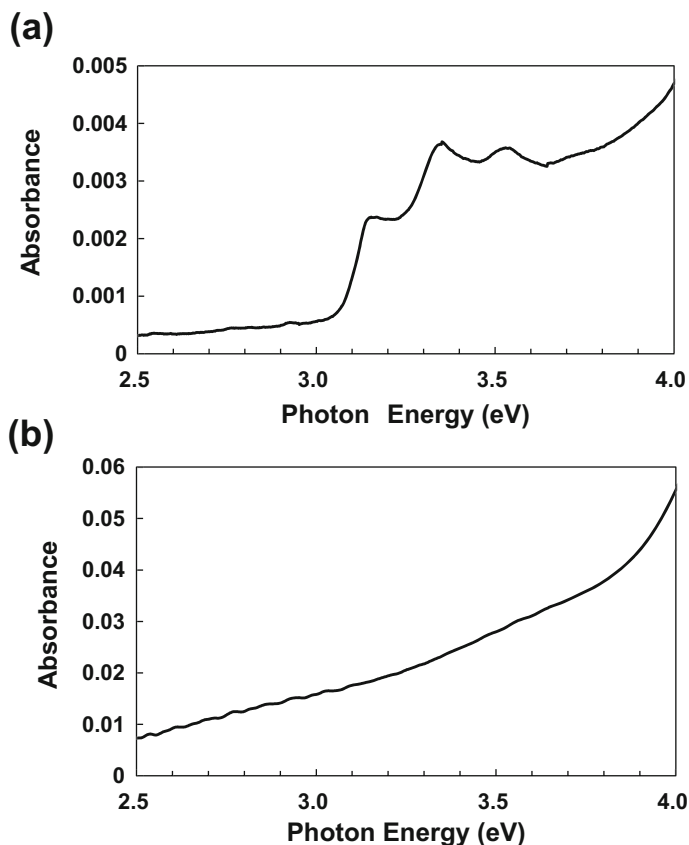


Fig. 9.11 Absorption spectra for the following specimens: (a) blue-PL Si nanopowder in hexane, (b) after addition of an HNO_3 +HF solution to specimen a

absorption spectrum of hexane containing DMA without Si nanopowder doesn't change at all by addition of the HF+ HNO_3 solution.

The peaked structure in the absorption spectra results from transition to the electronic excited-state with various vibrational states. The peaks at 3.153, 3.341, and 3.530 eV are due to (0,0), (1,0), and (2,0) bands. (For both the PL spectra and the absorption spectra, (l, m) denotes transition between the l-th vibrational state of the electronic excited-state and the m-th vibrational state of the electronic ground-state.) The separated energy for these peaks of 0.19 eV is ~ 0.02 eV higher than that observed without Si nanopowder. This result indicates that adsorbed DMA in the excited-state has a slightly higher C–C bond energy, possibly leading to a shorter C–C bond length than that of free DMA.

The shortened C–C bond length in the excited-state results in an increase in the difference in the bond length between the excited- and ground-states. The PL spectrum of free DMA molecules has a (0,0) peak with the highest intensity

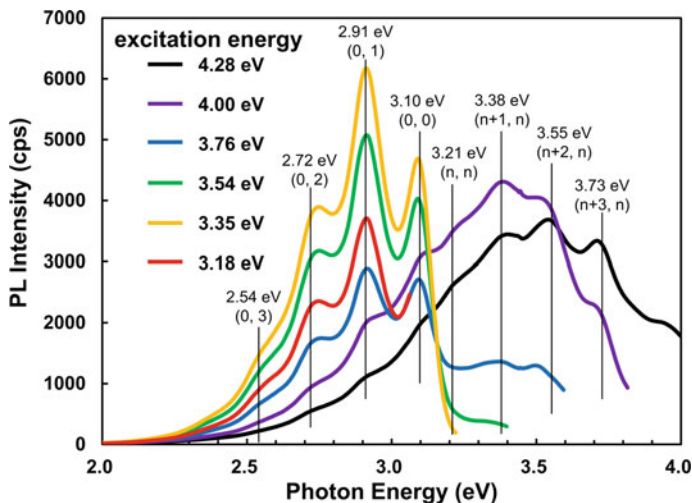


Fig. 9.12 PL spectra for blue-PL Si nanopowder in hexane observed with various excitation photon energies between 3.18 and 4.28 eV

(spectrum d in Fig. 9.9), which results from the nearly identical C–C bond lengths of DMA in the electronic ground- and excited-states. On the other hand, the PL spectra of DMA adsorbed on Si nanopowder possess the (0,1) peak with the highest intensity (spectra a~c in Fig. 9.9). This result is in accordance with the above consideration that the C–C bond length of adsorbed DMA in the excited-state is shorten.

Figure 9.12 shows the PL spectra of blue-PL Si nanopowder in hexane, i.e., DMA-adsorbed Si nanopowder, observed with various excitation energies. With the excitation energies higher than 3.76 eV, PL peaks with energies higher than the (0,0) band are observed at 3.21, 3.38, 3.55, and 3.73 eV, i.e., nearly the constant energy separation, in a broad peak. The energies of the sharp peaks remain constant by changing the excitation photon energy, while the broad peak shifts toward the higher energy with an increase in the excitation energy. The broad peak is attributed to band-to-band transition of Si nanopowder, similar to the case of green-PL (Figs. 9.5 and 9.7).

Each neighboring PL peak is separated by 0.17~0.18 eV, which is nearly identical to that observed in the absorption spectrum (Fig. 9.11). These PL peaks with energies higher than the (0,0) energy are attributable to transitions from the vibrational excited-states, and thus, the separation energy corresponds to the vibrational energy in the electronic excited-state, i.e., the same as that observed in the absorption spectra. The transition from the vibrational excited-states most probably results from an increased probability of the transition between the electronic excited-state and the ground-state, in analogy to electronic transition observed in absorption spectrum b of Fig. 9.11.

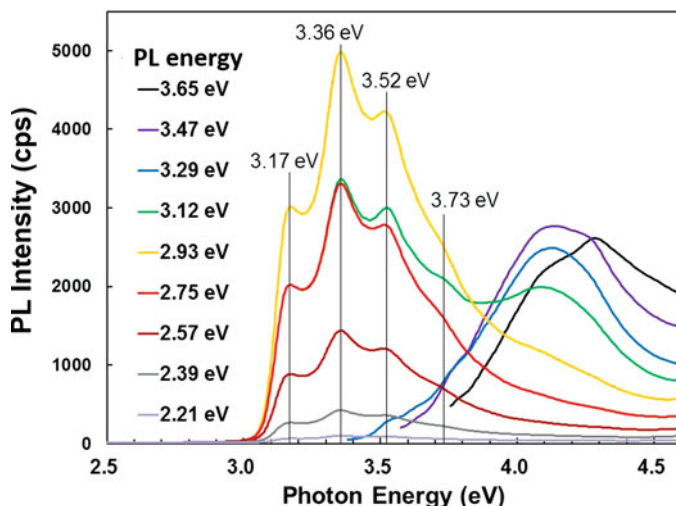


Fig. 9.13 PL excitation spectra for blue-PL Si nanopowder in hexane observed at various PL energies between 2.21 and 3.65 eV

Figure 9.13 shows the PL excitation spectra for blue-PL Si nanopowder in hexane. The excitation spectra are measured by scanning the incident photon energy with the PL energy fixed, and thus, they correspond to absorption which causes PL emission at the fixed PL energy. For the PL energies between 2.39 and 2.93 eV, i.e., transitions from the vibrational ground-state, peaked structure is observed, showing that absorption by adsorbed DMA causes the PL peaks. In the higher energy region, on the other hand, broad structure is present with no vibronic bands. The broad structure is attributable to absorption by Si nanopowder, indicating that the PL peaks with energies higher than the (0,0) peak result from band-to-band excitation of Si nanopowder.

Figure 9.14 shows the time-dependent PL intensity measured at 2.91 eV (curve a) and 3.35 eV (curve b). The PL intensity at 3.35 eV for DMA without Si nanopowder is shown in curve c for reference, and in this case, the PL lifetime is determined to be 5.0 ns. The PL lifetime measured at 2.91 eV which corresponds to the (0, 1) transition of DMA, on the other hand, is much shorter, i.e., 0.97 ns. Considering that the pulse width of incident light is 0.75 ns, the real lifetime is estimated to be 0.62 ns for DMA with Si nanopowder and 4.9 ns for DMA without Si nanopowder. The short lifetime results from the high PL transition probability, indicating that the interaction of DMA with Si nanopowder greatly increases the PL transition probability.

The PL energy for curve b (3.35 eV) corresponds to the (n+1, n) PL band overlapped with the more intense band-to-band transition of Si nanopowder. The lifetime considering the pulse width is estimated to be 3.1 ns, indicating that the lifetime of electron-hole pairs in Si nanopowder is much longer than the PL lifetime arising from adsorbed DMA of 0.62 ns.

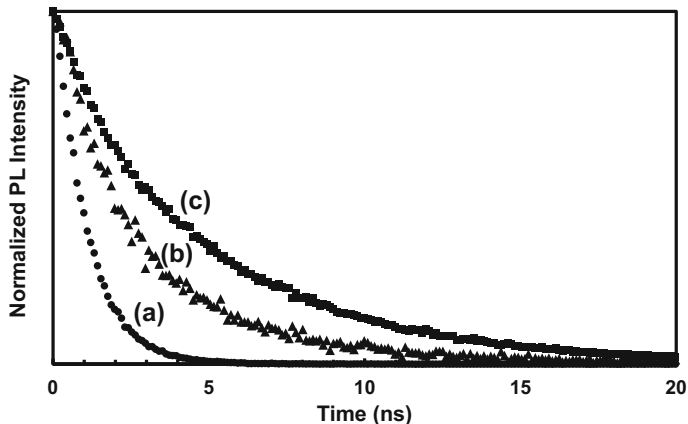


Fig. 9.14 Time-dependent PL intensity for blue-PL Si nanopowder in hexane measured with the following excitation photon energies: (a) 2.91 eV, (b) 3.35 eV. Curve c is for DMA-containing hexane without Si nanopowder

Photoluminescence Enhancement for DMA by Adsorption on Si Nanopowder

The absorption bands due to DMA appear in the presence of Si nanopowder in hexane, while they aren't observed in the absence of Si nanopowder (cf. Fig. 9.11). This result clearly shows that the light absorption probability is greatly increased by adsorption on Si nanopowder. Therefore, the PL enhancement is partly attributable to an increased light absorption probability.

The transition probability from the ground-state to the excited-state is greatly enhanced by adsorption of DMA on Si nanopowder as described above. Therefore, it is quite likely that the transition probability from the excited-state to the ground-state is also increased by the adsorption. The PL intensity is proportional to the product of the light absorption probability and the PL emission probability, leading to the great enhancement by $\sim 60,000$ times by adsorption of DMA on Si nanopowder (cf. Fig. 9.10).

The PL intensity, I_g , for transitions from vibrational ground-state of the electronic excited-state is proportional to the number of electrons, n_e , in the vibrational ground-state and the rate constant, k_r , for radiative transition. Considering the PL enhancement factor by Si nanopowder of 60,000, we have

$$I_g \propto n_e^1 k_r^1 = 60,000 n_e^0 k_r^0, \quad (9.3)$$

where superscripts 0 and 1 denote the values without and with Si nanopowder, respectively. For n_e^0 and n_e^1 , we have the following differential equations:

$$\frac{dn_e^0}{dt} = -\left(k_r^0 + k_{nr}^0\right)t, \quad (9.4)$$

$$\frac{dn_e^1}{dt} = -\left(k_r^1 + k_{nr}^1\right)t, \quad (9.5)$$

where k_{nr} is the rate constant for non-radiative transition. Since the PL lifetime is inversely proportional to the total rate constant, we have

$$4.9 : 0.62 = \frac{1}{k_r^0 + k_{nr}^0} : \frac{1}{k_r^1 + k_{nr}^1}. \quad (9.6)$$

Considering the quantum efficiency of 0.42 and 0.45 for PL in the absence and presence of Si nanopowder, respectively, we have

$$\frac{k_r^0}{k_r^0 + k_{nr}^0} = 0.42, \quad (9.7)$$

$$\frac{k_r^1}{k_r^1 + k_{nr}^1} = 0.45. \quad (9.8)$$

Using Eqs. (9.6), (9.7), and (9.8), we have

$$k_r^1 = 8.5k_r^0. \quad (9.9)$$

Therefore, using Eq. (9.3), n_e^1 is given by

$$n_e^1 = 7.1 \times 10^3 n_e^0. \quad (9.10)$$

The above consideration can lead to the following conclusion. The PL intensity is increased by adsorption on Si nanopowder for the following two reasons: (i) an increase in the number of electrons in the electronic excited-state (~ 7100 times enhancement) and (ii) an increase in the rate constant for radiative transition (~ 8.5 times enhancement). The increased number of electrons in the excited-state results from the increased transition probability which in turn results from a great increase in the dynamic dipole moment by adsorption and/or enhancement of wave function of DMA by adsorption, i.e., surface resonance state [25].

Photoluminescence Mechanism

The excitation spectra with the PL energies lower than 3.12 eV clearly possess vibronic bands (Fig. 9.13), indicating that adsorbed DMA molecules are directly excited. In the excitation spectra for the PL energies higher than 3.29 eV, on the other hand, a broad structure is dominant. The peak energy of the broad structure shifts in the higher energy direction with the PL energy. It should be noted that for excitation with energies higher than 3.76 eV, the PL vibronic bands from vibrational excited-states are observed (cf. Fig. 9.12). This result demonstrates that for PL emission from vibrational excited-states, incident light is absorbed

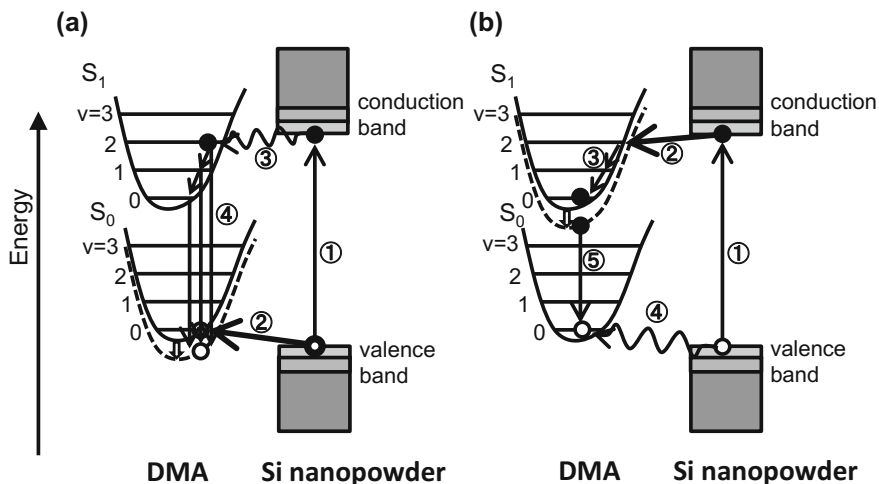


Fig. 9.15 Mechanism of blue-PL emission involving generation of electron-hole pairs in Si nanopowder by incident light, followed by electron and hole transfer to adsorbed DMA with the following order: (a) a photo-generated hole transfers to DMA first, (b) a photo-generated electron transfers to DMA first

by Si nanopowder. Therefore, it can be concluded that for PL emission from the vibrational excited-states, electron-hole pairs are generated in Si nanopowder, and they transfer to adsorbed DMA, followed by recombination.

The lifetime of photo-generated electron-hole pairs (3.1 ns) is much longer than the PL lifetime (0.62 ns), and therefore, a photo-generated electron and a hole transfer to adsorbed DMA separately. We consider the case where a photo-generated hole in Si nanopowder moves to adsorbed DMS first, and then an electron moves to DMA. In this case, the hole is captured by the potential of the electronic ground-state of DMA. The ground-state with a positive charge is stabilized due to solvation (Fig. 9.15a). Immediately when an electron is captured by a potential of the electronic excited-state, transition from the electronic excited-state to the ground-state occurs. Due to the high transition probability, transition from the vibrational excited-state to the electronic ground-state proceeds. Since solvation lowers the potential energy of the ground-state, the transition energy is increased by solvation, leading to a blue shift of the PL peaks.

For the opposite case, an electron generated in Si nanopowder transfers to adsorbed DMA first, followed by transfer of a hole to DMA (Fig. 9.15b). An electron is captured in the electronic excited-state of DMA, and in this case, internal relaxation to the vibrational ground-state proceeds before electronic transition because of the absence of a hole in the electronic ground-state. There is enough time for solvation of adsorbed DMA with the electron in the electronic excited-state to proceed before a hole transfers to DMA (Fig. 9.15b). Due to solvation, the potential energy of the electronic excited-state is lowered. When a hole transfers to DMA, it is captured in the vibrational ground-state of the electronic ground-

state. Immediately after a hole is captured, electronic transition of the electron in the electronic excited-state occurs, resulting in PL emission. Because of lowering of the potential energy for the temporary captured electron (i.e., the potential of the excited-state), the PL energy decreases, in contrast to the case where a hole transfers to DMA first. The above consideration clearly shows that the PL energy for case a in Fig. 9.15 increases by solvation, while that for case b decreases. This consideration is verified by observation of two (0, 0) bands (or one (0,0) band and one (n, n) band) separated by 0.11 eV. Each solvation energy is likely to be approximately a half of the energy difference of the two (0, 0) bands, i.e., ~ 55 meV.

The (0, 0) PL band for case a and the (n, n) band for case b are located at 3.10 and 3.21 eV, respectively. The (0, 0) band in the absorption spectra is observed at 3.15 eV, i.e., the average energy between the (0, 0) and (n, n) PL bands. In the case of light absorption, both the initial and final states are in neutral charge states, and therefore, solvation doesn't occur. Therefore, the transition energy is between that for the ground-state-stabilized case (case a) and the excited-state-stabilized case (case b).

The intensity ratios of the PL peaks due to transitions from the vibrational ground-states, i.e., (0, 0), (0, 1), (0, 2), and (0, 3) bands, are nearly independent on the excitation energy. This is because after complete internal relaxation, transition from the vibrational ground-state proceeds, and in this case, the PL intensity is determined by the individual Franck-Condon factors which don't depend on the excitation energy. On the other hand, the intensity ratios of the PL peaks due to transitions from the vibrational excited-states strongly depend on the incident photon energy. To explain this phenomenon, we consider the case where an electron enters the x -th vibrational state of the electronic excited-state. The n -th PL band contains various transitions, (l, m), which satisfy the following equation:

$$l - m = n. \quad (9.11)$$

The transition rate, $R_{l,m}$, is given by the product of the transition probability, $P_{l,m}$, and the number of electrons in the l -th vibrational state, N_l :

$$R_{l,m} = P_{l,m} N_l. \quad (9.12)$$

N_l is given by

$$N_l = N_x (1 - a_x) (1 - a_{x-1}) \cdots \cdots (1 - a_{l+1}) = N_x \prod_x^{l+1} (1 - a_x), \quad (9.13)$$

where N_x is the number of electrons transferred from Si nanopowder to the x -th vibrational state of the electronic excited-state, and a_j expresses the transition probability from the j -th vibrational states to various vibrational states of the electronic ground-state which probability is proportional to the sum of the Franck-Condon factors:

$$a_j \propto \sum_m F_{j,m}, \quad (9.14)$$

where $F_{j,m}$ is the Franck-Condon factor for the (j, m) transition. The term, $\prod_{j=x}^{l+1} (1 - a_j)$, in Eq. (9.13) expresses the probability that an electron transferred from Si nanopowder to the x -th vibrational state of adsorbed DMA relaxes to the l -th vibrational state without electronic transition. Therefore, we have

$$R_{l,m} \propto F_{l,m} \prod_j^{n-l+1} (1 - a_j) = F_{l,m} P_{l,m} N_x \prod_x^{l+1} (1 - a_x). \quad (9.15)$$

The intensity of the n -th band, I_n , is proportional to the sum of the transition rates over l which satisfies Eq. (9.11):

$$I_n \propto N_x \sum_l F_{l,l-n} \prod_j^{n-l+1} (1 - a_j) = N_x \sum_l P_{l,m} \prod_x^{l+1} (1 - a_x). \quad (9.16)$$

Equation (9.16) clearly shows that the PL intensity of the n -th band (i.e., $(a+n, a)$, $a = 0, 1, 2, 3 \dots$) depends not only on the Franck-Condon factor for the $(n, 0)$ transition, $F_{n,0}$, (i.e., $a = 0$), but also other Franck-Condon factors. When the incident photon energy is varied, the vibrational energy state, x , to which a photo-generated electron in Si nanopowder transfers, is changed, leading to a change in the PL intensity, I_n . Therefore, the PL bands whose intensities depend on the excitation energy support the transition from vibrational excited-states.

9.2 Hydrogen Generation from Si Nanopowder by Reaction with Water

9.2.1 Introduction

Reactive oxygen species (ROS) are generated in the body for various reasons, e.g., metabolism [26], UV irradiation [27], and environmental pollution [28]. Among ROS, hydroxyl radicals (OH radicals) possess the highest oxidation-reduction potential, i.e., the highest oxidation power. Oxidation of cells, DNA [29], lipid [30], etc., (i.e., oxidative stress) causes various diseases such as Alzheimer's disease [31, 32], Parkinson's disease [31, 33], chronic kidney failure [34], cancer cell proliferation [35], atopic dermatitis [36], cutaneous senility [37], etc. Hydrogen reacts with OH radicals to form water molecules, and thus hydrogen can prevent oxidative stress-induced diseases.

Although Si bulk doesn't strongly react with water in the neutral pH region between 7 and 9, Si nanopowder with sizes less than ~ 30 nm does, leading to

generation of hydrogen molecules [38–40]. Therefore, oral administration of Si is expected to prevent oxidative stress-induced diseases.

To prevent oxidative stress-induced diseases by elimination of OH radicals generated in the body without side effects, the following three requirements should be satisfied: (i) a large amount of reducing species is present in the body, (ii) the concentration of reducing species is always maintained high, and (iii) reducing species reacts only with OH radicals among ROS. Requirement (i) arises from the high reactivity of OH radicals, which easily attack and oxidize cells, and therefore, hydrogen is necessary to react with OH radicals before they damage cells. Requirement (ii) results from continuous generation of OH radicals in the body due to mitochondrial respiratory metabolism. Other ROSes possess physiological functions such as immunity, and therefore, their elimination may cause side effects. Hydrogen reacts only with the most reactive OH radicals among ROSes (requirement iii), and therefore, no side effects arise by hydrogen.

Hydrogen-rich water may have effects to prevent oxidative stress-induced diseases. However, the saturated hydrogen concentration in water is only 1.6 ppm at room temperature, and even in the case of the saturated concentration, only 18 mL hydrogen gas dissolves in 1 L water. The hydrogen concentration in hydrogen-rich water is usually much lower because hydrogen easily diffuses to air even when it is contained in a container. Moreover, in 1 h, the hydrogen concentration in every organ returns to the initial values before intake of hydrogen-rich water [41]. Therefore, the effects of intake of hydrogen-rich water on oxidative stress-induced diseases seem to be limited.

Polyphenol [42, 43], vitamin C [44], and vitamin E [45] can eliminate OH radicals. However, their reducing power is too strong to react with other ROSes. Therefore, taking a large amount of these species may cause side effects. Moreover, keeping a high concentration of these species in the body continuously is almost impossible.

We have demonstrated that the above three requirements can be satisfied with intake of Si composition, as explained below.

9.2.2 Experiments

Si nanopowder was fabricated from Si powder (Koujundo Chemical Laboratory, Si Powder ca. 5 μm) by use of the beads milling method with 0.5 mm Φ zirconia beads, unless otherwise noted. Fabricated Si nanopowder was etched in a 5wt% HF solution for 10 min at room temperature, followed by immersion in ethanol to make the surface hydrophilic.

For the reaction with water in the neutral pH region between 7 and 9, the generated hydrogen volume was obtained by measuring the hydrogen concentration in water using a TOA DKK DH-35A potable dissolved hydrogen meter, while that generated by the reaction with strong alkaline solutions was determined just by measuring the volume after subtraction of the volume of water vapor.

Fourier transform infrared absorption (FT-IR) spectra were measured using a JASCO FT/IR-6200 spectrometer. X-ray photoelectron spectroscopy (XPS) measurements were performed by use of a KRATOS AXIS-165x spectrometer with an Mg $K\alpha$ radiation source in which photoelectrons were collected in the surface-normal direction. SEM measurements were carried out using a JOEL JSM-6335F microscope.

9.2.3 Results and Discussion

9.2.3.1 Reaction of Si Nanopowder with Strong Alkaline Solutions

Figure 9.16 shows the hydrogen volume generated by the reaction of Si nanopowder with strong alkaline solutions having pH higher than 12.9 at room temperature. The total amounts of generated hydrogen are 1589 mL/g for the pH 13.9 solution, 1530 mL/g for the pH 13.4 solution, and 972 mL/g for the pH 12.9 solution. The maximum hydrogen generation rate in the case of the reaction with pH 13.9 solution is 351 mL/min.g. This hydrogen generation rate corresponds to $\sim 10,000$ times that for photocatalytic hydrogen generation using efficient photocatalysts such as Ta_3N_5/SiO_2 which respond to visible light [46]. Using the 1 g photocatalyst under AM1.5 100 mAW/cm² irradiation, generation of 1,500 mL hydrogen requires more than 1.5 years. In the case of Si nanopowder, $\sim 1,500$ mL hydrogen can be generated in a few minutes although the reaction is irreversible.

We consider the following reaction mechanisms for hydrogen generation by the reaction of Si nanopowder with water:

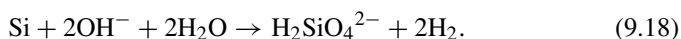
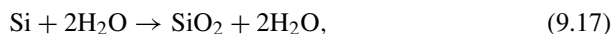
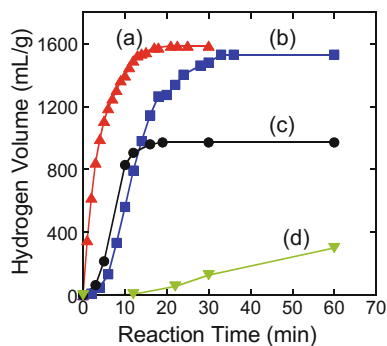


Fig. 9.16 Hydrogen volume generated by the reaction of Si nanopowder with alkaline solutions at room temperature having following pHs: (a) 13.9, (b) 13.4, (c) 12.9, (d) 12.1



Both the reactions generate 2 M hydrogen from 1 M Si, i.e., 1712 mL hydrogen at room temperature from 1 g Si. Reaction (9.17) doesn't consume OH^- ions, while reaction (9.18) does, resulting in a decrease in pH. Therefore, the reaction ratio, i.e., the hydrogen volume generated by reaction (9.18) divided by the total generated hydrogen volume, can be estimated from the decrease in pH. This ratio is estimated to be 1.0 for pH 13.4 and 13.9 solutions, 0.58 for pH 12.9 solutions, and 0.12 for pH 12.1 solutions. By reaction (9.18), soluble $\text{H}_2\text{SiO}_4^{2-}$ ions are formed, and thus, all Si atoms in Si nanopowder can react with OH^- ions because no materials to prevent the reaction with OH^- ions are present on the Si surface. For reaction (9.17), on the other hand, SiO_2 with low solubility is formed on the surface, and when the SiO_2 thickness reaches a certain value, the hydrogen generation stops because of the migration-limited mechanism. (For reaction (9.17), OH^- ions are the migrating species through SiO_2 as explained below.) We have observed that when the SiO_2 thickness reaches to ~ 5 nm, the hydrogen generation reaction stops. The decrease in the volume of generated hydrogen with a decrease in pH can be explained by this migration-limited mechanism.

1589 mL/g hydrogen generated by the reaction with pH 13.9 solutions is 93% of the stoichiometric value of 1712 mL/g at room temperature. This small difference is attributable to the presence of a silicon oxide layer on Si nanopowder before the hydrogen generation reaction, i.e., 7wt% Si is already oxidized before the reaction.

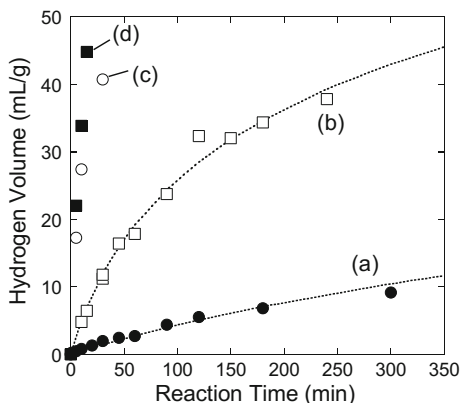
972 mL/g hydrogen is generated by the reaction with the pH 12.9 solutions, which is equal to 61% hydrogen generated by the reaction with 13.9 solutions, and therefore, unreacted Si is estimated to be 39% that before the reaction. The weight of SiO_2 formed by the hydrogen generation reaction is estimated to be 1.22 g from initial 1 g Si nanopowder. Assuming that Si nanopowder before the reaction possesses spherical shape with the 23.4 nm diameter (i.e., the average diameter before the reaction), the diameter of unreacted Si nanopowder is estimated to be 17.1 nm. From the diameter of unreacted Si nanopowder, its weight, and the weight of formed SiO_2 , the thickness of formed SiO_2 is estimated to be 5.1 nm, in good agreement with that estimated from XPS measurements, i.e., 4.8 nm.

9.2.3.2 Reaction of Si Nanopowder with Neutral Water

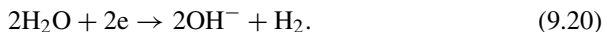
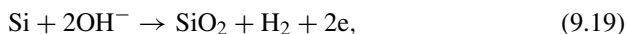
Si nanopowder was produced from Si powder for hydrogen generation experiments with neutral water. The size of Si nanopowder is larger than that produced from Si swarf, i.e., for one-step milling, the mode diameter, the median diameter, and the average diameter are 6.6, 14.0, and 23.4 nm, respectively, and those for two-step milling are 5.8, 9.6, and 13.8 nm, respectively.

Figure 9.17 shows the hydrogen volume generated by the reaction with water in the neutral pH region vs. the reaction time. Even in the case of the reaction with ultrapure water of pH 7.0, Si nanopowder generates hydrogen (plot a), but the hydrogen generation rate is low, i.e., $0.026\sim 0.047$ mL/min.g. The hydrogen generation rate increases by the reaction with tap water having pH 7.4 (plot b). The hydrogen generation rate further increases by increases of pH to 8.0 (plot c) and 8.6

Fig. 9.17 Hydrogen volume generated from Si nanopowder vs. the reaction time for the reaction with water having following pHs: (a) 7.0 (ultrapure water), (b) 7.4 (tap water), (c) 8.0, (d) 8.6



(plot d). The initial hydrogen generation rates for pH 7.4, 8.0, and 8.6 solutions are higher by approximately 10, 50, and 100 times than that for ultrapure water of pH 7.0. On the other hand, the change in pH observed after the hydrogen generation reaction is much lower than that calculated assuming that OH^- ions are consumed for the hydrogen generation reaction. (The slight pH change is due to dissolution of CO_2 in the air to the solutions during the hydrogen generation reaction.) From these results, the most probable reaction schemes are written as



In reaction (9.19), Si reacts with OH^- ions, forming SiO_2 , H_2 , and electrons most probably in the SiO_2 conduction band. Electrons transfer to the SiO_2 surface, and water molecules accept them, resulting in the formation of OH^- ions and H_2 . OH^- ions are consumed in reaction (9.19) but generated in reaction (9.20), and therefore, after the overall reaction (reaction (9.17) = reactions (9.19) + (9.20)), the concentration of OH^- ions, i.e., pH, doesn't change. The reaction rate for reaction (9.19) is much lower than that for reaction (9.20), and therefore, the total reaction rate greatly increases with the concentration of OH^- ions.

If reaction (9.19) was the rate-determining step for hydrogen generation reaction, then the reaction rate should be proportional to the square of the concentration of OH^- ions. However, the initial reaction rates for the reaction with pH 7.4, 8.0, and 8.6 solutions are approximately 10, 50, and 100 times that for ultrapure water of pH 7.0. It is very likely that even in the early reaction stage, a silicon oxide layer is present on Si nanopowder, and migration of OH^- ions through the oxide layer is the rate-determining step, as explained below.

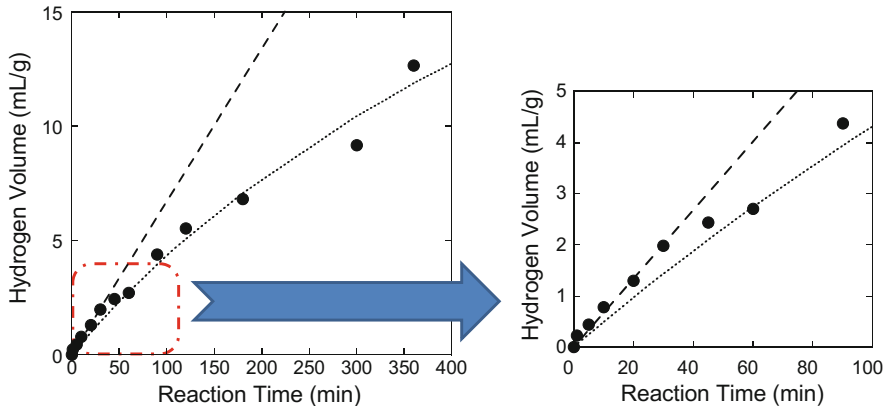


Fig. 9.18 Hydrogen volume generated from Si nanopowder vs. the reaction time for the reaction with ultrapure water. The dashed and dotted lines show the calculated curves for the reaction-limited and migration-limited mechanisms

Figure 9.18 shows the generated hydrogen volume vs. the reaction time for the reaction of Si nanopowder with ultrapure water of pH 7.0 at room temperature. The observed plot is well expressed by the curve calculated with the following procedure: Si nanopowder is assumed to possess spherical shape with the initial diameter, r_0 , and the diameter changes to $r_1(t)$ by the hydrogen generation reaction. The weight of an SiO_2 overlay, W_{ox} , is simply written as

$$W_{\text{ox}} = \frac{4\pi}{3} (r_o^3 - r_1^3) D_{\text{Si}} \frac{60}{28}, \tag{9.21}$$

where D_{Si} is the density of Si nanopowder. Using the SiO_2 thickness, l_{ox} , W_{ox} is given by

$$W_{\text{ox}} = \frac{4\pi}{3} [(r_1 + l_{\text{ox}})^3 - r_1^3] D_{\text{ox}}, \tag{9.22}$$

where D_{ox} is the density of silicon oxide. The hydrogen volume generated from unit weight Si nanopowder, V_{H_2} , is given by

$$V_{H_2} = \frac{4\pi}{3} [(r_1 + l_{\text{ox}})^3 - r_1^3] D_{\text{ox}} \frac{3}{4\pi r_0^3 D_{\text{Si}}} C_0 = \frac{[(r_1 + l_{\text{ox}})^3 - r_1^3]}{r_0^3} \frac{D_{\text{ox}}}{D_{\text{Si}}} C_0, \tag{9.23}$$

where C_0 is a constant.

When anions are the moving species through SiO_2 and their migration is the rate-determining step, the relationship between the SiO_2 thickness, l_{ox} , and the reaction time, t , is given by [47]

$$l_{\text{ox}} = \frac{kT}{C_1} \ln \frac{C_1 C_2 (t + t_0)}{kT} - \frac{W}{C_1}, \quad (9.24)$$

where W is the activation energy for migration of anions, and C_1 and C_2 are constants. Using Eqs. (9.23) and (9.24), the relationship between the generated hydrogen volume, V_{H_2} , and the reaction time, t , can be calculated, and the result is shown by the dotted line in Fig. 9.18.

In cases where the reaction at the Si/SiO₂ interface is the rate-determining step, the relationship between the SiO₂ thickness, l_{ox} , and the reaction time, t , is simply given by

$$l_{\text{ox}} = Ct, \quad (9.25)$$

where C is a constant. Using Eqs. (9.23) and (9.25), the relationship between V_{H_2} and t can be obtained, and the calculated curve is shown by the dashed line in Fig. 9.18. The experimental plot in the initial reaction stage and the subsequent stage is well fitted by the dashed line and the dotted line, respectively. This result shows that in the initial reaction stage, interfacial reaction is the rate-determining step, and in the subsequent stage, anions, i.e., OH⁻ ions, are the migrating species, and the migration of OH⁻ ions through SiO₂ is the rate-determining step. The rate-determining step changes from the interface reaction to migration of OH⁻ ions across silicon oxide at the generated hydrogen volume between 2.0 and 2.2 mL/g. In the case of the reaction with pH 8.0 and 8.6 solutions (plots c and d in Fig. 9.17), this volume of hydrogen is generated in a few minutes, showing that the rate-determining step changes to migration in the very early reaction stage.

For reaction (9.19), OH⁻ ions move inward, while for reaction (9.20), electrons move outward. This mechanism in which negative charges transfer in the opposite direction is likely to decrease the activation energy for migration of OH⁻ ions which is the rate-determining step. By this decrease in the activation energy, the hydrogen generation reaction proceeds easily at room temperature, resulting in the formation of the thick silicon oxide layer of ~5 nm thickness. It should be noted that in the case of thermal oxidation of crystalline Si, formation of a ~5 nm SiO₂ layer requires temperatures above 700 °C [48].

Figure 9.19 shows the hydrogen volume generated by the reaction of HF-etched Si nanopowder with ultrapure water vs. the reaction time for two different crystallite sizes. The hydrogen generation rate for smaller crystallite size Si nanopowder produced by the two-step beads milling method (average crystallite size: 13.8 nm) is 1.4~1.5 times higher than that for the larger crystallite size Si nanopowder (average crystallite size 23.4 nm). The surface area estimated from the average crystallite size is 190 m²/g for the two-step beads milled Si nanopowder and 110 m²/g for the one-step beads milled Si nanopowder. The ratio of the hydrogen generation rate of 1.4~1.5 between the two-step and one-step beads milled Si nanopowders is in reasonable agreement with the ratio of the surface area estimated from the average crystallite sizes. Si nanopowder forms agglomerate as is evident from the SEM micrograph (Fig. 9.20). The average sizes of Si agglomerates for one-step

Fig. 9.19 Hydrogen volume vs. the reaction time for the reaction of Si nanopowder fabricated by the following methods with ultrapure water: (a) one-step beads milling (average crystallite diameter: 23.4 nm), (b) two-step beads milling (average crystallite diameter: 13.8 nm)

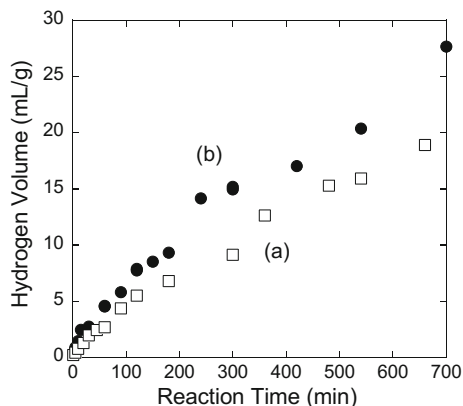
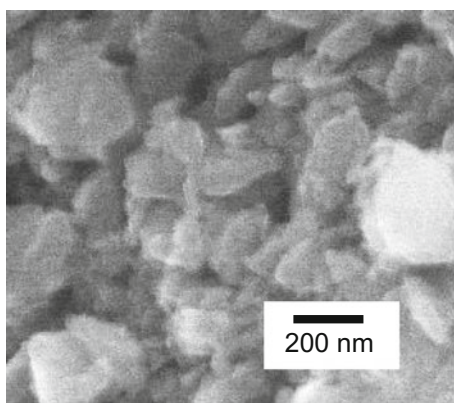


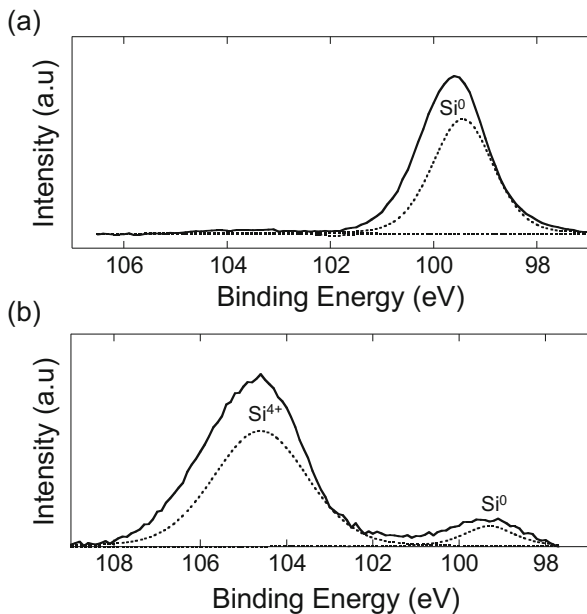
Fig. 9.20 SEM micrograph of Si nanopowder fabricated by the one-step beads milling method



and two-step beads milled Si nanopowders determined from dynamic light scattering measurements are nearly the same, i.e., 128 and 134 nm, respectively. These results show that the hydrogen generation rate strongly depends on the crystallite size but not on the size of agglomerate.

The thickness of the silicon oxide layer formed on Si nanopowder by the reaction with water is estimated from XPS spectra in the Si 2p region (Fig. 9.21). The peak at 99~100 eV is due to Si nanopowder, and the broader peak centered at 103~105 eV is attributable to silicon oxide [49, 50]. After HF etching (spectrum a), the peak due to silicon oxide is very weak, and the thickness of the oxide layer is thought to be less than 0.3 nm. When the hydrogen generation reaction stops after the reaction with pH 8.0 solutions for 24 h, the thickness of the silicon oxide layer can be estimated assuming a cylindrical shape with the radius, R , the same as the height. (Although Si nanopowder possesses polygonal shape (cf. Fig. 9.1.), assumption of cylindrical shape is thought not to cause a serious error in estimation of the silicon oxide thickness.) In this case, the oxide thickness, l_{ox} , is estimated using the following equation [51]:

Fig. 9.21 XPS spectra in the Si 2p region for Si nanopowder fabricated by the one-step beads milling method: (a) after etching with an HF solution, (b) after the reaction of specimen a with the pH 8 solution for 24 h



$$\frac{I_{\text{ox}}}{I_{\text{Si}}} = \frac{N_{\text{ox}}\sigma_{\text{ox}}\lambda_{\text{ox}}}{N_{\text{Si}}\sigma_{\text{Si}}\lambda_{\text{Si}}} \frac{(R - l_{\text{ox}})^2 \left[1 - \exp\left(-\frac{l_{\text{ox}}}{\lambda_{\text{ox}}}\right) \right] + l_{\text{ox}}(2R - l_{\text{ox}}) \left[1 - \exp\left(-\frac{R}{\lambda_{\text{ox}}}\right) \right]}{(R - l_{\text{ox}})^2 \exp\left(-\frac{l_{\text{ox}}}{\lambda_{\text{ox}}}\right) \left[1 - \exp\left(-\frac{R - l_{\text{ox}}}{\lambda_{\text{Si}}}\right) \right]}, \quad (9.26)$$

where I is the area intensity of the XPS peak; N , σ , and λ are the number density of Si atoms, the photoemission cross-section, and the photoelectron mean free path, respectively; and subscripts, ox and Si , denote the values for silicon oxide and Si, respectively. The radius, R , is assumed to be 11.7 nm which is a half of the average diameter determined from XRD measurements. In this estimation, the following values are adopted: $\lambda_{\text{ox}} = 2.9$ nm for Mg $K\alpha$ (1254 eV) radiation, $\lambda_{\text{Si}} = 2.5$ nm, and $\frac{\sigma_{\text{ox}}}{\sigma_{\text{Si}}} = 1.1$ [52, 53]. Using Eq. (9.26), the silicon oxide thickness after the hydrogen generation reaction stops (spectrum b) is determined to be 4.8 nm.

Figure 9.22 schematically shows the mechanism of hydrogen generation from Si nanopowder. OH^- ions are adsorbed on the silicon oxide surface. OH^- ions migrate through a silicon oxide layer (step 1) enhanced by electrical field induced by adsorbed OH^- ions. Si atoms at the Si/silicon oxide interface react with OH^- ions, leading to generation of hydrogen, silicon oxide, and electrons in the conduction band of the silicon oxide layer (step 2). Electrons in the conduction band move outward to the silicon oxide surface (step 3), and then, electrons are accepted by water molecules, generating OH^- ions and hydrogen (step 4). Namely, OH^- ions move inward, while electrons move outward, which is likely to decrease the activation energy of inward migration of OH^- ions, i.e., the rate-determining

Fig. 9.22 Schematic mechanism of the reaction of Si nanopowder with water in the neutral pH region

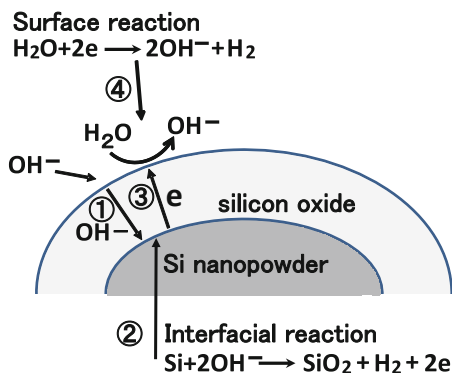
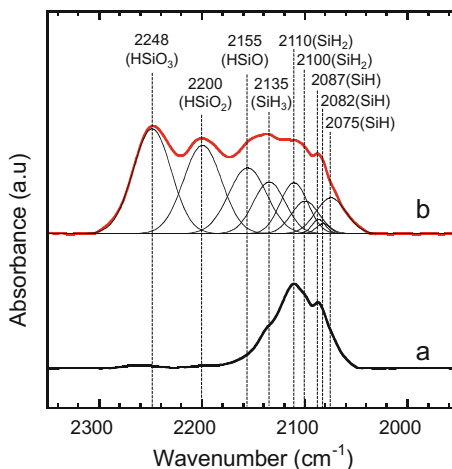


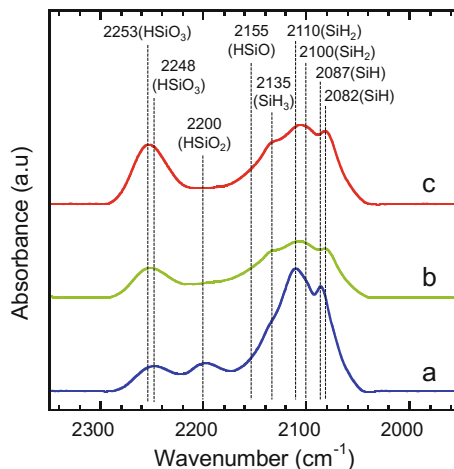
Fig. 9.23 FT-IR spectra in the Si-H stretching vibrational region for HF-etched Si nanopowder: (a) just after etching with the HF solution, (b) after the reaction of specimen a with ultrapure water for 24 h



step for the hydrogen generation reaction from Si nanopowder, and therefore, the reaction proceeds at room temperature.

The initial reaction of HF-etched Si nanopowder with ultrapure water is investigated using FT-IR spectroscopy (Fig. 9.23). HF-etched Si nanopowder exhibits three peaks in the Si-H stretching vibrational region (spectrum a), and they are attributed to SiH (2087 cm⁻¹), SiH₂ (2110 cm⁻¹), and SiH₃ (2155 cm⁻¹) [54, 55]. After reaction with ultrapure water for 24 h at room temperature (spectrum b), new peaks appear at 2158, 2200, and 2248 cm⁻¹, which are attributable to HSiO, HSiO₂, and HSiO₃ species, respectively [56, 57], and the peaks due to SiH, SiH₂, and SiH₃ are still present. These results show that OH⁻ ions attack Si back bonds to form Si-O bonds, but they don't attack Si-H bonds. Nearly the same energy differences between the HSiO and HSiO₂ peaks and between the HSiO₂ and HSiO₃ peaks show that only one species with one hydrogen atom (i.e., HSiO, HSiO₂, and HSiO₃, but not H₃SiO, H₂SiO, and H₂SiO₂) is included in each Si-H stretching vibrational peak.

Fig. 9.24 FT-IR spectra in the Si-H stretching vibrational region for HF-etched Si nanopowder after the reaction with pure heavy water for the following periods: (a) 10 min, (b) 3 h, (c) 24 h



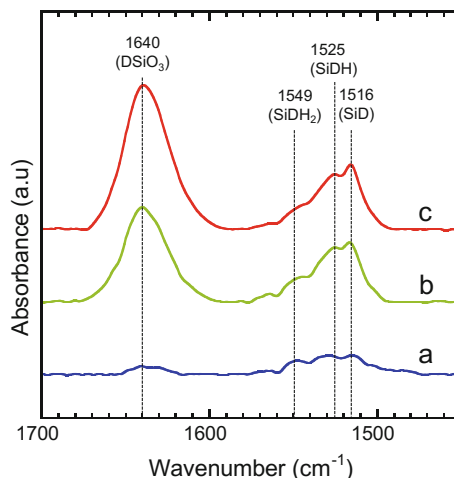
In the case of the reaction with pure D_2O (Fig. 9.24), a strong $HSiO_3$ peak is observed even after 10 min reaction, but the intensity of the peak due to $HSiO_2$ is much weaker (spectrum a), and after 3 h reaction, the intensity of the $HSiO_3$ peak increases, while the $HSiO_2$ peak disappears almost completely (spectrum b). This result is in strong contrast to the reaction with H_2O where $HSiO_2$ species is present even after the reaction for 24 h (spectrum b in Fig. 9.23). This difference can be explained by the local reaction to form two-dimensional agglomerate-like structure in the case of the surface reaction with D_2O , while the reaction proceeds more uniformly on the surface for the reaction with H_2O .

The peak due to $HSiO_3$ shifts from 2248 (cf. spectrum a for 10 min reaction) to 2253 cm^{-1} (spectrum c for 24 h reaction) with the reaction time for the reaction with D_2O , while such a shift doesn't occur in the case of the reaction with H_2O . This shift is most probably attributable to an increase of the charge on Si atoms [58]. Namely, the Si-H bonds become stronger as the reaction proceeds locally. For the reaction with H_2O , on the other hand, the reaction proceeds uniformly, and such a change in the charge state doesn't occur.

After the reaction with D_2O , vibrational peaks are observed in the Si-D stretching vibrational region (Fig. 9.25), indicating that replacement of H atoms to D atoms proceeds on the surface. Peaks appear at 1516 , 1525 , and 1549 cm^{-1} , and they are most probably attributable to SiD , $SiDH$, and $SiDH_2$ species, respectively. The replacement probability after 24 h reaction (spectrum c) is estimated to be 37%, and therefore, the probabilities of formation of SiD_2 and SiD_2H (or SiD_3) are likely to be much lower than those of $SiDH$ and $SiDH_2$, respectively.

Although the intensity of the Si-H peak is lower than that of Si- H_2 peak before the reaction with D_2O (spectrum a in Fig. 9.23), the intensity of the Si-D peak is higher than that of the Si-DH peak after the reaction with D_2O . This result indicates that Si-H bonds in Si-H species are weaker than those in Si- H_2 species, resulting

Fig. 9.25 FT-IR spectra in the Si-D stretching vibrational region for HF-etched Si nanopowder after the reaction with pure heavy water for the following periods: (a) 10 min, (b) 3 h, (c) 24 h



in the higher replacement probability. This result is in accordance with the higher frequency of the Si-H₂ vibrational peak than that of the Si-H peak.

After the reaction with D₂O for 3 h (spectrum b), a strong peak due to DSiO₃ is observed at 1640 cm⁻¹, while no peak due to DSiO₂ is present. This result also indicates the formation of agglomerate-like structure which consists of DSiO₃ and HSiO₃.

9.3 Conclusion

Si nanopowder is fabricated by use of the beads milling method. Fabricated Si nanopowder has the following PL and hydrogen generation characteristics:

1. Si nanopowder etched with an HF solution and immersed in ethanol shows green-PL. The PL energy depends on the excitation photon energy, and it is attributed to band-to-band transition of Si nanopowder whose band-gap is enlarged by the quantum confinement effect.
2. Si nanopowder which isn't etched with HF and immersed in hexane exhibits blue-PL. The PL energy is independent of the excitation photon energy, and it is attributed to transition of DMA adsorbed on Si nanopowder.
3. The intensity of blue-PL is enhanced by ~60,000 times due to adsorption of DMA on Si nanopowder. The PL intensity is increased by adsorption on Si nanopowder for the following two reasons: (i) an increase in the number of electrons in the electronic excited-state (~7100 times enhancement) and (ii) an increase in the rate constant for radiative transition (~8.5 times enhancement).

4. For blue-PL arising from excitation with energies higher than 3.76 eV, PL peaks with energies higher than the (0,0) band are present, and they are attributed to transition from vibrational excited-states.
5. The excitation spectra show that blue-PL results from the two different mechanisms: (i) excitation of adsorbed DMA and (ii) band-to-band transition of Si nanopowder, followed by transfer of photo-generated electrons and holes to DMA. For mechanism (ii), a photo-generated electron and a hole transfer to DMA separately, resulting in two (0,0) bands.
6. Only when a photo-generated hole transfers to DMA first, followed by electron transfer, transition from vibrational excited-states occurs.
7. Si nanopowder easily reacts with strong alkaline (pH>13) solutions, and almost stoichiometric amount of hydrogen (i.e., ~1700 mL/g) is generated in a few minutes.
8. Si nanopowder reacts with water in a neutral pH region between 7 and 9 to generate hydrogen. In this case, the hydrogen generation rate markedly increases with pH of the solution, while pH doesn't change by the reaction. In the first reaction stage, Si nanopowder reacts with OH⁻ ions, generating hydrogen, silicon oxide, and electrons in the conduction band of silicon oxide, while in the second reaction stage, electrons are accepted by water molecules to form hydrogen and OH⁻ ions.
9. In the very early hydrogen generation reaction stage (less than 2.2 mL/g hydrogen generation), the surface reaction is the rate-determining step, and then, migration of OH⁻ ions through a silicon oxide layer becomes the rate-determining step.
10. The hydrogen generation reaction stops when a ~5 nm silicon oxide layer is formed on Si nanopowder.
11. The hydrogen generation rate strongly depends on the crystallite size of Si nanopowder, but it doesn't depend on the size of its agglomerate.

9.4 Outlook

Si is a nontoxic material, and its medical application is expected. We have proposed two kinds of medical application of Si nanopowder, i.e., (i) photoluminescence material and (ii) internal hydrogen generation material. For application (i), Si nanopowder can be applied to life cell imaging, e.g., to detect cancer cells. Si nanopowder, especially, blue-PL Si nanopowder, can give much stronger PL than conventional dyes and is more stable, especially, high photostability, both of which make the application easier and more effective.

For various diseases, oxidation stress is one of the largest factors to cause diseases. Hydrogen generation in the body can decrease oxidative stress, and therefore, it can prevent various oxidative stress-induced diseases. Moreover, for apparently healthy persons, i.e., persons who don't suffer from diseases but on whom addition of a tiny factor causes diseases, a decrease of oxidative stress can

make them really healthy. The decrease of oxidative stress by internal hydrogen generation can also retard aging, which can extend health life expectancy.

Si-based agent which can generate a high amount of hydrogen in bowels is now being developed in our laboratory. Contrary to conventional medicines, Si-based agent isn't absorbed in the body, but only hydrogen generated from the agent is absorbed. Therefore, a medicine with great medical effects but without any side effects is expected to be developed using Si-based agent.

References

1. N. O'Farrell, A. Houlton, B.R. Horrocks, *Int. J. Nanomed.* **1**, 451 (2006)
2. Z. Kang, Y. Liu, C.H.A. Tsang, D.D.D. Ma, X. Fan, N.-B. Wong, S.-T. Lee, *Adv. Mater.* **21**, 661 (2009)
3. X.P. Zhu, T. Yukawa, M. Hirai, T. Suzuki, H. Suematsu, W. Jiang, K. Yatsui, *Appl. Surf. Sci.* **242**, 256 (2005)
4. M. Inada, H. Nakagawa, I. Umezu, A. Sugimura, *Mater. Sci. Eng.* **B101**, 283 (2003)
5. L. Mangolini, *J. Vac. Sci. Technol. B* **31**, 020801 (2013)
6. O.B. Gusev, A.N. Poddubny, A.A. Prokofiev, I.N. Yassievich, *Semiconductors* **47**(2), 183–202 (2013)
7. Z. Gu, X.-Y. Chen, Q.-D. Shen, H.-X. Ge, H.-H. Xu, *Polymer* **51**, 902 (2010)
8. E. Fazio, F. Barreca, S. Spadaro, G. Currò, F. Neri, *Mater. Chem. Phys.* **130**, 418 (2011)
9. K. Watanabe, K. Sawada, M. Koshiba, M. Fujii, S. Hayashi, *Appl. Surf. Sci.* **197–198**, 635 (2002)
10. L. Nikolova, R.G. Saint-Jacques, C. Dahmoune, G.G. Ross, *Surf. Coat. Technol.* **203**, 2501 (2009)
11. P.T. Huy, V.V. Thu, N.D. Chien, C.A.J. Ammerlaan, J. Weber, *Physica B* **376–377**, 868 (2006)
12. C. Lam, Y.F. Zhang, Y.H. Tang, C.S. Lee, I. Bello, S.T. Lee, *J. Crystal Growth* **220**, 466 (2000)
13. Y.V. Ryabchikov, S.A. Alekseev, V. Lysenko, G. Bremond, J.-M. Bluet, *J. Nanopart. Res.* **15**, 1535 (2013)
14. M. Imamura, J. Nakamura, S. Fujimasa, H. Yasuda, H. Kobayashi, Y. Negishi, *Eur. Phys. J. D* **63**, 289 (2011)
15. Y.C. Fang, Y. Zhang, H.Y. Gao, L.G. Chen, B. Gao, W.Z. He, Q.S. Meng, C. Zhang, Z.C. Dong, *Appl. Surf. Sci.* **285P**, 572 (2013)
16. T. Matsumoto, M. Maeda, H. Kobayashi, *Nanoscale Res. Lett.* **11**, 7 (2016)
17. M. Maeda, T. Matsumoto, H. Kobayashi, *Phys. Chem. Chem. Phys.* **19**, 21856 (2017)
18. T. Matsumoto, M. Maeda, J. Furukawa, W.-B. Kim, H. Kobayashi, *J. Nanopart. Res.* **16**, 2240 (2014)
19. M. Maeda, K. Imamura, T. Matsumoto, H. Kobayashi, *Appl. Surf. Sci.* **312**, 39 (2014)
20. T. Ida, S. Shimazaki, H. Hibino, H. Toraya, *J. Appl. Cryst.* **36**, 1107 (2003)
21. G. Conibeer, Silicon nanocrystals, Pavesi and R. Turan (eds.), Wiley-VCH Verlag GmbH & Co. KGaA, Weinheim, pp. 555–561, 2010.
22. J.P. Wilcoxon, G.A. Samara, P.N. Provencio, *Phys. Rev. B* **60**, 2704 (1999)
23. K. Ohno, *Chem. Phys. Lett.* **53**, 571 (1978)
24. A. Henßge, J. Acker, C. Müller, *Talanta* **68**, 581 (2006)
25. K. Oura, V.G. Lifshits, A.A. Saranin, A.V. Zotov, and M. Katayama, *Surface Science*, Springer, Berlin/Heiderberg/New York, p. 267, 2003.
26. D.R. Johar, L.H. Bernstein, *Diab. Res. Clin. Pract.* **126**, 222 (2017)
27. K. Takeshita, C. Chi, H. Hirata, M. Oho, T. Ozawa, *Free Radic. Biol. Med.* **40**, 876 (2006)

28. B. Shao, L. Mao, N. Qu, Y.-F. Wang, H.-Y. Gao, F. Li, L. Qin, J. Shao, C.-H. Huang, D. Xu, L.-N. Xie, C. Shen, X. Zhou, B.-Z. Zhu, *Free Radic. Biol. Med.* **104**, 54 (2017)
29. J.B. Jeong, E.W. Seo, H.J. Jeong, *Food Chem. Toxicol.* **47**, 2135 (2009)
30. Y. Hayashi, Y. Ueda, A. Nakamura, H. Yokojyama, Y. Mitsuyama, H. Ohya-Nishiguchi, H. Kamada, *Brain Res.* **941**, 107 (2002)
31. T. Jian, Q. Sun, S. Chen, *Prog. Neurobiol.* **147**, 1 (2016)
32. J. Li, C. Wang, J.H. Zhang, J.M. Cai, Y.P. Cao, X.J. Sun, *Brain Res.* **1328**, 152–161 (2010)
33. A. Yoritaka, M. Takanashi, M. Hirayama, T. Nakahara, S. Ohta, N. Hattori, *Mov. Disord.* **28**, 836 (2013)
34. O. Boutaud, L.J. Roberts II, *Free Radic. Biol. Med.* **51**, 1062 (2011)
35. A. Kagawa, K. Katsura, M. Mizumoto, Y. Tagawa, Y. Masiko, *Mater. Sci. Forum* **706–709**, 520 (2012)
36. Y.S. Yoon, M.E. Sajo, R.M. Ignacio, S.K. Kim, C.S. Kim, K.J. Lee, *J. Biol. Pharm. Bull.* **37**, 1480 (2014)
37. S. Kato, Y. Saitoh, K. Iwai, N. Miwa, J. Photochem. Photobiol. B Biol. **106**, 24 (2012)
38. Y. Kobayashi, S. Matsuda, K. Imamura, H. Kobayashi, *J. Nanopart. Res.* **19**, 176 (2017)
39. K. Imamura, Y. Kobayashi, S. Matsuda, T. Akai, H. Kobayashi, *AIP Adv.* **7**, 085310 (2017)
40. Y. Kobayashi, K. Imamura, T. Matsumoto, H. Kobayashi, *J. Elect. Eng.* **68**, 17 (2017)
41. C. Liu, R. Kurokawa, M. Fujino, S. Hirano, B. Sato, X.-K. Li, *Sci. Rep.* **4**, 5485 (2014)
42. G.K.B. Lopes, H.M. Schulman, M. Hermes-Lima, *Biochim. Biophys. Acta* **1472**, 142 (1999)
43. S. Ozgová, J. Heřmánek, I. Gut, *Biochem. Pharmacol.* **66**, 1127 (2003)
44. D.D. Kitts, *Trends Food Sci. Technol.* **8**, 198 (1997)
45. E. Niki, *Free Radic. Biol. Med.* **66**, 3 (2014)
46. X. Liu, L. Zhao, K. Domen, K. Takanabe, *Mater. Res. Bull.* **49**, 58 (2014)
47. D.D. Eley, P.R. Wilkinson, *Proc. R. Soc. London Ser. A* **254**, 327 (1960)
48. A. Atkinson, *Rev. Mod. Phys.* **57**(2), 437 (1985)
49. F.J. Himpfel, F.R. McFeely, A. Taleb-Ibrahimi, J.A. Yarmoff, G. Hollinger, *Phys. Rev. B* **38**, 6084 (1988)
50. H. Kobayashi, T. Ishida, Y. Nakato, H. Tsubomura, *J. Appl. Phys.* **69**, 1736 (1991)
51. O. Renault, R. Marlier, N.T. Barrett, E. Martinez, T. Baron, M. Gely, B. De Salvo, *Surf. Interface Anal.* **38**, 486 (2006)
52. H. Kobayashi, Asuha, O. Maida, M. Takahashi, H. Iwasa, *J. Appl. Phys.* **94**, 7328 (2003)
53. M.F. Hochella Jr., A.H. Carim, *Surf. Sci.* **197**, L260 (1988)
54. A.I. Belogorokhov, S.A. Gavrilov, P.K. Kashkarov, I.A. Belogorokhov, *Phys. Status Solidi A* **202**, 1581 (2005)
55. Y.H. Ogata, T. Tsuboi, T. Sakka, S. Naito, *J. Porous Mater.* **7**, 63 (2000)
56. Y. Kato, T. Ito, A. Hiraki, *Jpn. J. Appl. Phys.* **27**, L1406 (1988)
57. X.H. Sun, S.D. Wang, N.B. Wong, D.D.D. Ma, S.T. Lee, *Inorg. Chem.* **42**, 2398 (2003)
58. G. Lucovsky, *Solid State Commun.* **29**, 571 (2017)